Journal of Nuclear Materials 618 (2026) 156207

Contents lists available at ScienceDirect

Journal of Nuclear Materials

journal homepage: www.elsevier.com/locate/jnucmat

Irradiation tolerant medium-entropy multilayer films with interface optimization mechanism

Li Jiang [a], Jiannan Hao [b], Guanzhi Wang [a], Guang Ran [c,*], Yanhui Li [a], Qing Peng [b,d,e,*], Wei Zhang [a,*], Lumin Wang [f,*]

[a] School of Materials Science and Engineering, Dalian University of Technology, Dalian 116024, China
[b] The State Key Laboratory of Nonlinear Mechanics, Institute of Mechanics, Chinese Academy of Sciences, Beijing 100190, China
[c] College of Energy, Xiamen University, Xiamen 361002, China
[d] Center of Materials Science and Optoelectronics Engineering, University of Chinese Academy of Sciences, Beijing 100049, China
[e] Guangdong Aerospace Research Academy, Guangzhou 511458, China
[f] Department of Nuclear Engineering and Radiological Sciences, University of Michigan Ann Arbor, MI 48109, USA

HIGHLIGHTS

- The hetero phase interfaces act as defect sinks, facilitating annihilation and recombination in nanoscale multilayer film.
- The bubbles tend to distribute along Type 1 (K-S: (011^{-})BCC || $(11^{-}1)$FCC, $[1^{-}11]$BCC || [011]FCC) interface in Cu layers.
- The average segregation energy is lower in Type 1 (−2.8 eV) than those in Type 2 (−2 eV), thus leading to the aggregation of vacancies.

GRAPHICAL ABSTRACT

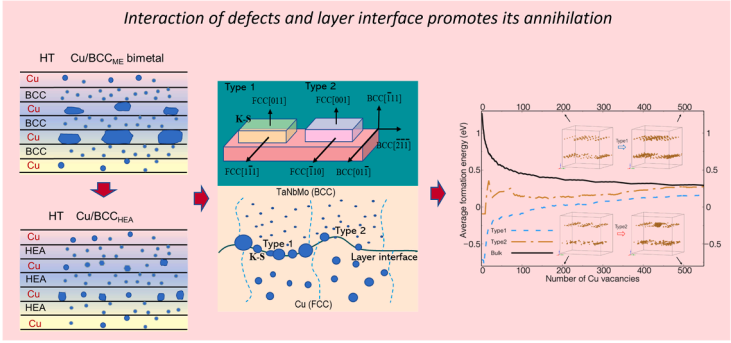

ARTICLE INFO

Keywords:
Nuclear energy
Cladding materials
Multilayer films
Medium-entropy alloys
Irradiation resistance

ABSTRACT

Irradiation induced helium damage is harmful in nuclear energy, thus irradiation resistant materials are highly desirable. Nanostructuring is an advanced strategy to mitigate the helium damage with pre-exist defects. In this work, we have investigated the irradiation effects in Cu/($Ta_{50}Nb_{25}Mo_{25}$) medium-entropy multilayer films using experiments accompanied with molecular dynamics simulations. The multilayers with modulation period of 5 and 50 nm have been irradiated with 60 keV He ions at 300 and 400 °C, respectively, with total fluence of 10^{21} ions/m^2. The multilayers exhibit commendable microstructural stability, with the four constituent elements maintaining their intended modulation distribution after irradiation. A diverse range of bubble sizes is observed within the Cu layers, with sizes peaking at 3 to 5 nm in the region of maximal damage. However, bubbles with a diameter around 1 nm are detected in the $Ta_{50}Nb_{25}Mo_{25}$ layers, indicating that the bubbles are in the nucleation phase. The 50 nm multilayer shows two types of layer interfaces, i.e., $(01\bar{1})_{BCC}$ || $(1\bar{1}1)_{FCC}$, $[\bar{1}11]_{BCC}$ || $[011]_{FCC}$ (Type 1, K-S relationship), and $(01\bar{1})_{BCC}$ || $(\bar{1}10)_{FCC}$, $[\bar{1}11]_{BCC}$ || $[001]_{FCC}$ (Type 2). Bubbles tend to distribute along the Type 1 interface, molecular dynamics results suggest that the average formation energy of vacancy

* Corresponding authors.
E-mail addresses: gran@xmu.edu.cn (G. Ran), pengqing@imech.ac.cn (Q. Peng), wzhang@dlut.edu.cn (W. Zhang), lmwang@umich.edu (L. Wang).

https://doi.org/10.1016/j.jnucmat.2025.156207
Received 10 July 2025; Received in revised form 2 September 2025; Accepted 3 October 2025
Available online 3 October 2025

clusters in Type 1 is lower than that in Type 2, which is consistent with the trend of the monovacancy. As a result, the swelling rate of the medium-entropy multilayers is significantly decelerated compared with the bimetal multilayers.

1. Introduction

Helium ion irradiation would facilitate the formation of He bubbles in metals due to their minimal solubility within the metal matrix. The formation of these bubbles has been linked to structural swelling, surface exfoliation, embrittlement, and dimensional instabilities [1–3], leading to a notable deterioration in the physical and mechanical properties of alloys [4–6]. Therefore, mitigating the adverse effects of He irradiation-induced defects on the performance of structural materials poses a significant challenge in the application of nuclear energy.

The abundance of grain boundaries and interfaces in metals offers trapping sites for He, thereby delaying the nucleation and growth of He bubbles [7–9]. Nanoscale materials are promising candidates for nuclear applications except that they usually exhibit poor thermal stability, i.e., the grains may grow easily after high temperature irradiation. In contrast to nanocrystalline materials, multilayer films composed of immiscible elements in adjacent layers demonstrate superior thermal stability, characterized by negligible solid solubility of the components at elevated temperatures [10–13]. Additionally, these materials exhibit enhanced irradiation resistance due to the high-density layer interfaces that effectively trap and neutralize irradiation-induced defects. The various crystal structure combinations of multilayer films, including FCC/FCC, BCC/BCC, FCC/HCP, and BCC/HCP etc., demonstrate interesting characteristics compared to bulk metals. Especially, the FCC/BCC multilayers with discontinuous slip systems and immiscible interfaces can effectively serve as strong barriers to the transmission of dislocations, keeping excellent structural stability during high temperature and irradiation. Misra et al. [14–16] found that the Cu/Nb multilayer film showed thermal stable interfaces, and the interfaces of immiscible sublayers deferred the growth of the He bubbles. Zhang et al. [17,18] discovered that the interfaces of the immiscible Cu/V multilayers were capable of absorbing and reducing the concentration of irradiation-induced point defects effectively.

These reported efforts predominantly focused on multilayers composed of two pure metals. On the other hand, the swift advancement of multi-component alloys encompassing medium-entropy alloys and high-entropy alloys ((MEAs, HEAs) [19,20] provides an opportunity for developing novel multilayer films. Notably, multi-component alloys usually exhibit exceptional properties, including high thermal stability [21,22], superior corrosion resistance [23,24], excellent high-temperature strength and hardness [25], and outstanding irradiation resistance [26–30]. Therefore, combining the material design of multilayers and HEAs/MEAs holds great promise for applications in the nuclear energy.

In our previous work, we found that the Cu/($Ta_{50}Nb_{25}Mo_{25}$) MEA multilayer film exhibits immiscible layer interfaces [31]. Specifically, the 5 nm and 50 nm multicomponent multilayers demonstrate superior strength and plasticity compared to their bimetallic counterparts of equivalent layer thicknesses, which is attributed to the synergistic strengthening effect of solid solutions within the multicomponent layers. These distinctive properties render it promising for applications in the nuclear field. Based on this, the present study prepared Cu/($Ta_{50}Nb_{25}Mo_{25}$) MEA via DC magnetron sputtering and investigated its response to helium irradiation. The distribution of He bubbles along layer interfaces was examined to elucidate their interaction with irradiation-induced defects. The elemental diffusion after irradiation was detected to reveal microstructural stability. Additional nanoindentation studies were carried out to assess irradiation hardening induced by helium implantation. The nucleation and evolution of He bubbles and their interaction with layer interfaces were analyzed using molecular dynamics (MD) simulations. These findings are expected to provide insights into controlling the irradiation-induced defects in multilayer film materials.

2. Experimental

2.1. Synthesis and experimental procedures

Cu/($Ta_{50}Nb_{25}Mo_{25}$) multilayer film was deposited on Si substrates by magnetron co-sputtering technique [31]. The elemental proportion in $Ta_{50}Nb_{25}Mo_{25}$ MEA refers to the atomic percentage. $Ta_{50}Nb_{25}Mo_{25}$ layer was abbreviated as TaNbMo in the following text. Four targets with Cu, Ta, Nb, Mo pure metal were used for deposition. Ta, Nb, Mo targets worked together during deposition, which were opened intermittently with Cu target. The purity of each target was higher than 99.9 wt. % and the size of each target was Φ50.8 × 6.35 mm. Direct current (DC) magnetron sputtering was used to prepare the MEA multilayer films. The chamber was evacuated to 3.6×10^{-6} Pa before deposition and then maintained at 1 Pa by ventilating with argon during deposition. Each multilayer film contains modulation period of 5 and 50 nm, respectively. The total film thickness was approximately 1 μm. The MEA multilayer films show a superior uniformity, with a low surface roughness and uniform microstructure, the SEM images taken on the film surface can be seen in Fig. S1. Irradiation experiments were carried out at 300 and 400 °C, respectively, using a He ion beam with an irradiation energy of 60 keV and the fluence of 1×10^{21} ions/m^2 by accelerator at Xiamen Facility. The SRIM (Stopping and Ranges of Ions in Matter) software was used to estimate the irradiation damage during 60 keV He^+ irradiation, employing the quick Kinchin-Pease option [32]. The displacement energy (*Ed*) of all atoms was fixed as 40 eV [33].

The cross-sectional TEM samples were meticulously prepared using the FIB lift-out technique on an FEI Helios Nanolab workstation. Irradiation-induced defects were characterized using TEM (Cs-corrected JEOL 2100F). Helium bubbles were visualized using through-focus imaging technology. The helium bubble density was calculated based on the number of per unit volume. The sample thickness was measured using electron energy loss spectroscopy (EELS). ImageJ software was used to count the sizes and numbers of the cavities in the microstructures. The densities of the cavities were calculated using the following equation: $\rho = N/(A \times \delta)$, where N denotes the numbers of the cavities in the measured area; A denotes the statistical area; δ denotes the sample thickness. The elemental composition analysis was conducted using energy dispersive spectroscopy (EDS) detectors. The hardness was measured using a Bruker Hysitron TI950 Triboindenter equipped with a Berkovich probe. Each indentation test was performed on the top surface of the film under displacement control mode, with the maximum displacement set to 150 nm to minimize the substrate effect. The maximum load for each sample was determined based on the properties of the films. For each sample, a minimum of 10 indentations were conducted to ensure the reliability of the measurements.

2.2. Molecular dynamics simulations

For the simulation, Ta metal is employed as a proxy for the ternary TaNbMo alloy. First, the valence electron concentration of Ta closely matches the weighted average of the ternary alloy, ensuring that the electronic interaction characteristics at the Cu/MEA interfaces remain representative. Second, the monovacancy formation energies of Ta (2.82 eV), Nb (2.77 eV), and Mo (2.74 eV) exhibit minimal variation, in contrast to the significantly lower value for Cu (1.09 eV) [34]. This

Table 1
The lattice orientation and interface energy of the Ta/Cu interfaces.

Interface	bcc Ta	fcc Cu	γ (mJ/m^2)
Type 1	$X[1\bar{1}0]$, $Y[11\bar{2}]$, $Z[111]$	$X[111]$, $Y[\bar{1}\bar{1}2]$, $Z[1\bar{1}0]$	922.49, 1023.10 [39]
Type 2	$X[1\bar{1}0]$, $Y[11\bar{2}]$, $Z[111]$	$X[110]$, $Y[\bar{1}10]$, $Z[001]$	980.74
K-S	$X[111]$, $Y[\bar{1}\bar{1}2]$, $Z[1\bar{1}0]$	$X[1\bar{1}0]$, $Y[11\bar{2}]$, $Z[111]$	205.77, 206.97 [40]

difference provides a mechanistic explanation for the experimentally observed preferential nucleation of helium bubbles in Cu layers. Third, the similar mechanical properties and crystal structures of Ta, Nb, and Mo play a dominant role in interfacial dislocation and bubble interactions. Consequently, as the lack of available quaternary interatomic potentials, this simplified approach retains the essential interfacial physics. The atomistic Ta/Cu interface structures were constructed. MD calculations were carried out by LAMMPS package [35]. The Ta-Cu forcefield [36] was adopted to describe the interatomic interactions. Interface energies, vacancy formation energies, and segregation energies were determined. The detailed orientations of Ta/Cu interfaces are shown in Table 1. The boundary conditions with periodicity were employed along all the three-dimensions. An interface separation of 5 nm was maintained to preclude interface-image interactions. The interfaces were annealed for 10 ps under NPT ensemble (isothermal-isobaric ensemble) at 1000 K with pressure maintained at 0 Pa and uniformly cooled down to 0 K for another 10 ps under the same ensemble. The interface energy (γ) is defined as,

$$\gamma = \frac{E^{GB} - n_{Ta}E_c^{Ta} - n_{Cu}E_c^{Cu}}{2A} \quad (1)$$

where E^{GB} is the total interface energy, n_{Ta} and n_{Cu} represent the numbers of Ta and Cu atoms in the box, respectively. E_c^{Ta} and E_c^{Cu} represent the cohesive energy of BCC Ta and FCC Cu, and A is the area of the interface. We focus on Type 1 and Type 2 interfaces in this work. The interface energies are consistent with previous works employed the same interaction potential [37,38] (Table 1).

To evaluate the formation energy of a vacancy, the monovacancy configuration was created by removing a Cu or Ta atom in the interface and relaxed until the external force reaches zero ($< 10^{-15}$ eV/Å). The growth of the vacancy cluster was simulated via deleting atoms with the highest potential energy among the neighbor atoms. The formation energy of a vacancy or vacancy cluster ($E_f^{\alpha,\beta}$) is calculated by,

$$E_f^{\alpha,\beta} = E_{tot}^{\alpha,\beta} - E_{pft}^{\beta} + n_\alpha E_c^\alpha \quad (2)$$

where $E_{tot}^{\alpha,\beta}$ represents the total energy of an α-type vacancy (α = Ta or Cu) in β configuration (β = Type1, Type2, FCC Cu, or BCC Ta), E_c^α represents the cohesive energy of bulk α crystal, n_α represents the vacancy number, and E_{pft}^{β} is the total energy of the perfect β configuration without any defect. The segregation energy of a vacancy in the Ta/Cu interface ($E_s^{\alpha,\beta}$) can be evaluated by,

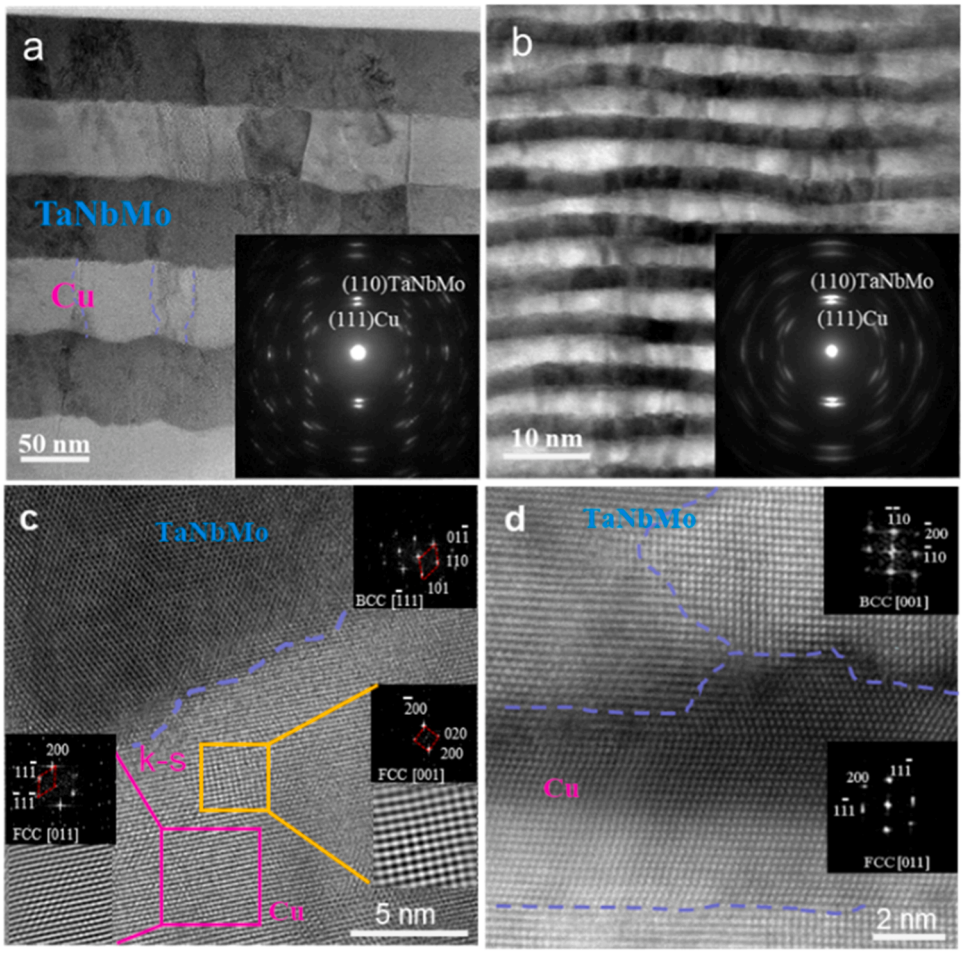

Fig. 1. Cross-sectional BF-STEM micrographs, HRTEM micrographs and FFT patterns of the MEA multilayer films. **(a, c)** 50 nm multilayer film, showing two types of interface relationships. (**b, d)** 5 nm multilayer film, showing the incoherent characteristic of layer interface.

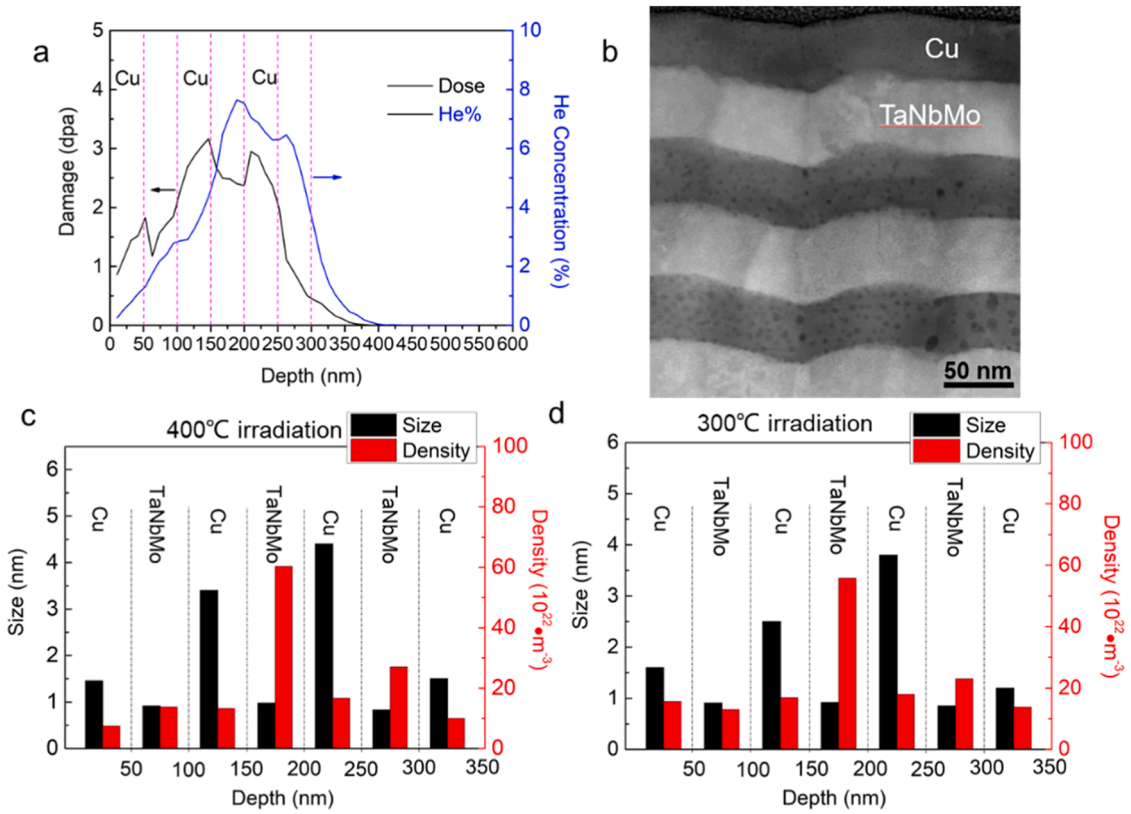

Fig. 2. Theoretical He concentration and practical He bubble distribution. **(a)** Depth profiles of damage and implanted He concentration calculated for Cu/TaNbMo 50 nm multilayer films after irradiated with 60 keV He^+ to fluence of 1×10^{21} ions/cm^2. **(b)** Cross-sectional bubble distribution of sample irradiated at 400 °C. **(c, d)** Average density and size of helium bubbles along irradiation depth of samples irradiated 400 °C and 300 °C, respectively.

$$E_s^{\alpha,\beta} = E_f^{\alpha,\beta} - E_f^{\alpha,bulk} \quad (3)$$

where $E_f^{\alpha,\beta}$ represents the formation energy of a vacancy or vacancy cluster. $E_f^{\alpha,bulk}$ represents the vacancy formation energy in bulk Ta or Cu. In other words, the segregation energy was calculated by the formation energy difference of a vacancy in the interface with that in bulk crystal. The negative sign of the segregation energy indicated a thermodynamic stability of the defect. The average formation or segregation energy was calculated by the formation or segregation energy divided by the number of vacancies, respectively.

3. Results and discussion

3.1. Microstructures of as-deposited multilayer films

The scanning TEM images of as-deposited Cu/TaNbMo multilayer films with modulation period of 50 and 5 nm are shown in Fig. 1(a) and (b), respectively. The selected-area diffraction patterns (SADP) confirm the mixed FCC and BCC structures with a polycrystalline texture in both films. The high-resolution TEM (HRTEM) images and corresponding Fast Fourier Transform (FFT) in Fig. 1(c) and (d) indicate that Cu layers illustrate an FCC structure, whereas the TaNbMo layers exhibit BCC structure. The 50 nm multilayer shows two types of interface: $(01\bar{1})_{BCC}$ || $(1\bar{1}1)_{FCC}$, $[\bar{1}11]_{BCC}$ || $[011]_{FCC}$ (Kurdjumov-Sachs relationship: K-S), and $(01\bar{1})_{BCC}$ || $(\bar{1}10)_{FCC}$, $[\bar{1}11]_{BCC}$ || $[001]_{FCC}$, respectively (see Fig. 1(c)). Fig. 1(d) illustrates a junction where three crystalline grains meet, displaying an incoherent interface characteristic, consistent with the behavior observed in bimetal multilayers with FCC/BCC layer interfaces [41].

3.2. Microstructural evolution

The implantation direction of He ions is perpendicular to the film surface. The damage and implanted ion concentration profiles of the Cu/TaNbMo 50 nm multilayer film are shown in Fig. 2(a). The cross-sectional STEM image of sample irradiated at 400 °C is shown in Fig. 2(b). Results suggest that a concentration peak appears at the depth of about 150 to 200 nm underneath the free surface, corresponding to TaNbMo layer. However, from Fig. 2(b), no obvious bubbles can be observed in this area, indicating the excellent irradiation resistance of TaNbMo layer at this temperature compared to Cu layer. In addition, since the growth rate of He bubbles is related to the homologous temperature (T_h) [42,43], $T_h = T/T_m$ (where T_m is thermodynamic melting temperature). Therefore, with the present implantation condition, bubbles prefer to grow in Cu ($T_h = 0.50$) compared to TaNbMo ($T_h = 0.22$).

The dose peaks appear at a depth of about 100 to 150 nm, and 200 to 250 nm, respectively, corresponding to Cu layers. Meanwhile, the He concentration in the area of 200 to 250 nm is relatively high. The average bubble size and density distributions along the irradiation depth of the 400 °C irradiated sample are shown in Fig. 2(c), from which it can be seen that bubbles in the area described above display a large size. The sample after 300 °C irradiation displays the same tendency, as shown in Fig. 2(d). It is observed that as the irradiation temperature increases, the bubble size increases at the same depth. In the area of 100–150 nm and 200–250 nm, the bubble size increases from 2.5 to 3.4 nm and 3.8 to 4.4 nm, respectively, when increasing irradiation temperature from 300 to 400 °C. However, increasing irradiation temperature leads to the decreased bubble density at the same depth, attributing that the bubbles in Cu layers are easier to migrate and coalesce at higher temperature. For Cu layers, in the area of 100–150 nm, the bubble density decreases from 16.9 to 13.3 $\times 10^{22}$ /m^3 when increasing irradiation temperature

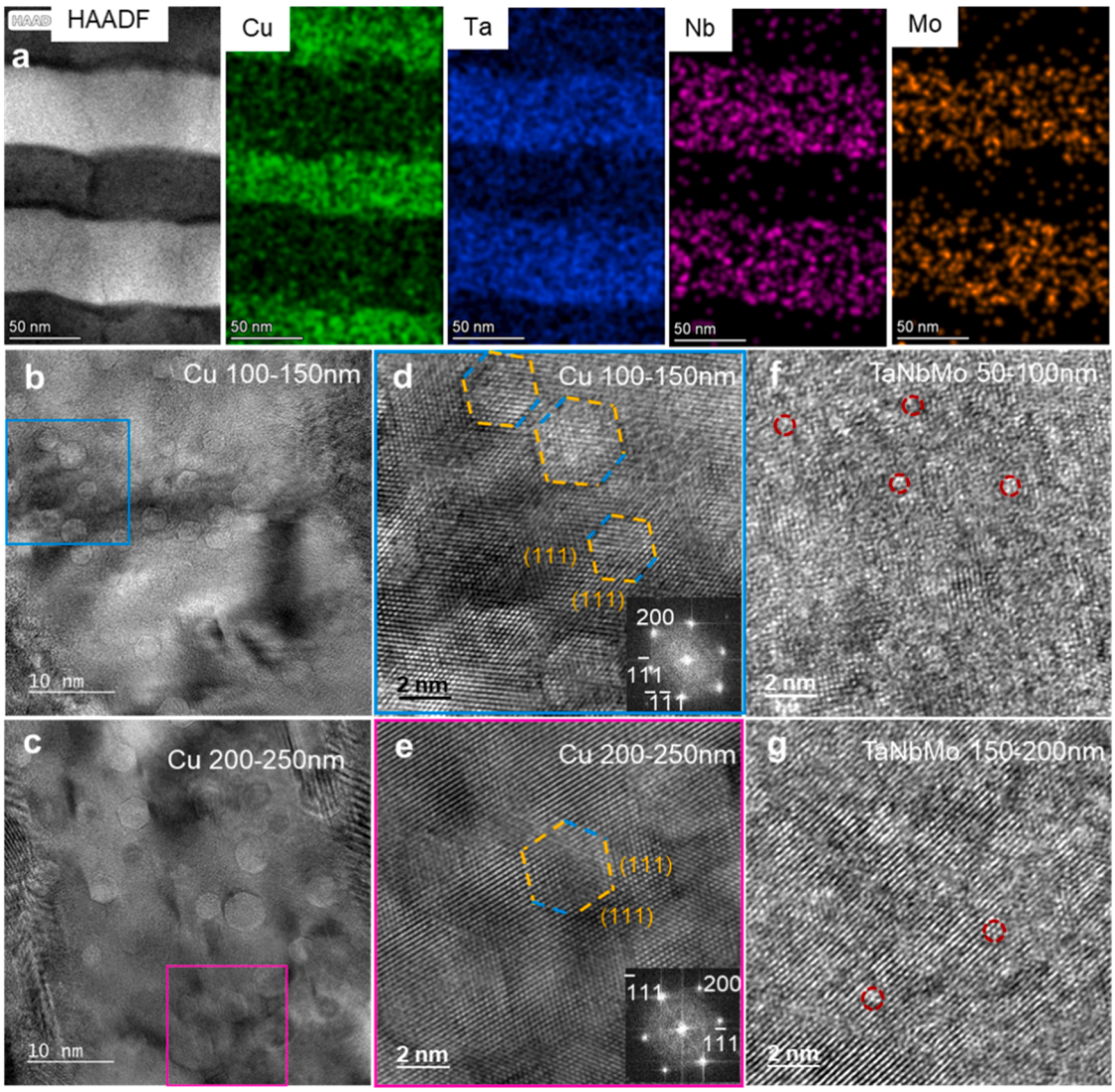

Fig. 3. Cross-sectional TEM images of 50 nm Cu/ TaNbMo multilayer films after He irradiation at 300 °C. **(a)** TEM image and EDS mapping, showing the elements are distributed as per the intended modulation, indicating the excellent microstructural stability. (**b, c)** Cu layer, 100–150 nm and 200–250 nm depth, respectively, showing the tendency of bubbles aligning along grain boundaries in the Cu layer. (**d, e)** The magnified images of the framed areas in b and c, respectively, displaying faceted bubbles in Cu layer, suggesting more vacancies are being absorbed by the bubbles. (**f, g)** TaNbMo layer, 50–100 nm and 150–200 nm depth, respectively, showing bubbles with 1 nm diameter distributing evenly.

from 300 to 400 °C, and in the area of 200–250 nm, the bubble density decreases from 18.0 to 16.7 $\times$ 10^{22} /m^3, respectively, as shown in Fig. 2 (c and d).

However, in both samples irradiated at 300 °C and 400 °C, the bubble size of the TaNbMo layers is maintained around 1 nm independent of irradiation depth, which indicates that the bubbles are in the stage of nucleation. But in the range of helium concentration peak, i.e., 150–200 nm depth, the bubble density is even higher, which can reach 55.8 $\times$ 10^{22} /m^3 and 60.3 $\times$ 10^{22} /m^3, respectively for the samples irradiated at 300 °C and 400 °C. Since the high helium concentration promotes the bubble nucleation, yet the bubble mobility is insufficient to facilitate their coalescence and growth.

To assess the microstructural stability of the 50 nm multilayer, an EDS mapping analysis was conducted across the peak damage zone and the peak helium concentration zone on the 300 °C irradiated samples (Fig. 3(a)). The analysis reveals that the elements are distributed as per the intended modulation, with the exception of Cu, which exhibits slight diffusion into adjacent layers. Overall, the 50 nm multilayers display a good microstructural stability under irradiation. The magnified microstructures of 100–150 nm and 200–250 nm depth of 50 nm multilayer film irradiated at 300 °C are shown in Fig. 3(b) and (c), respectively. The tendency of bubbles aligning along grain boundaries in the Cu layer is confirmed in Fig. 3(b). The magnified image of framed area in Fig. 3(b) is shown in Fig. 3(d), which displays faceted bubbles in Cu layer, suggesting more vacancies are absorbed by the bubbles.

The faceted bubble is still the main feature in the depth of 200–250 nm (Fig. 3(e)). Owing to the periodicity of the lattice, cavities exhibit faceting, with their facets aligned along close-packed planes. However, if the surface energy is modified by gas adsorption or if the gas pressure reaches a sufficiently high threshold, the cavities will adopt a spherical geometry. Notably, very large voids also tend toward a spherical shape, as the contribution of faceting diminishes with increasing void radius [44]. The facet planes appear to be $(100)_{Cu}$ and $(111)_{Cu}$ because of the low energy of free surface, i.e., 1.13 J/m^2 and 1.06 J/m^2, respectively [45–47]. In the depth range of 200–250 nm, with increasing He concentration, the average bubble size increases to 4.5 nm compared with that of 3.8 nm in depth of 100–150 nm. Considering TaNbMo layers, the small bubbles with average size of 0.9 nm in depth of 50–100 nm and 1.0 nm in depth of 150–200 nm can be seen in Fig. 3(f) and (g). The observations highlight a pronounced asymmetry in He bubble morphology

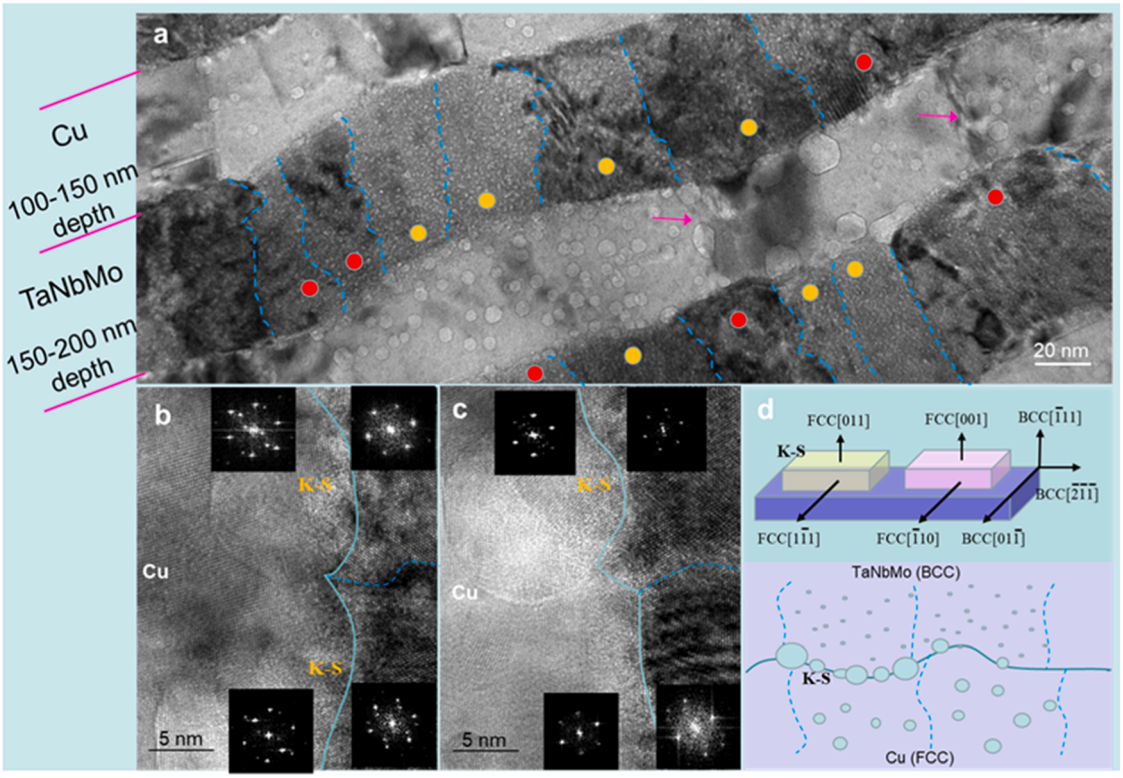

Fig. 4. Microstructure of samples irradiated at 400 °C. **(a)** Microstructure around 100–250 nm depth, showing the crystallographic orientation relationships of the FCC and BCC layer interfaces influence the bubble distribution. (**b, c)** Magnified microstructures of the FCC and BCC layer boundaries, showing the bubbles prefer to distribute along K-S type layer boundaries. The yellow circle marked layer interfaces conform to the K-S orientation relationship, while the red circle marked interfaces are type 2. (**d)** Schematic diagram of the bubble distribution tendency with the interface orientation relationship.

and distribution between the Cu and TaNbMo layers after He implantation at elevated temperatures: a wide range of bubble sizes is observed in Cu layers, while the TaNbMo layers contain bubbles with diameters averaging around 1 nm. This is because the bubbles in the TaNbMo layers are predominantly in the nucleation stage.

Fig. 4 shows the microstructure of 50 nm Cu/TaNbMo multilayer film irradiated at 400 °C. Fig. 4(a) captured at an irradiation depth of approximately 100–250 nm, reveals a bubble distribution pattern akin to that observed at 300 °C, characterized by larger bubbles in the Cu layer and smaller ones in the TaNbMo layer. Based on reported studies on bimetallic multilayer films and MEA multilayer films [12,16–18], both the MEA component itself and the interlayer interfaces contribute to enhancing irradiation resistance. It has been established that lattice distortion and chemical complexity in MEAs significantly reduce the mean free path of electrons, phonons, and magnons; this effect can alter defect formation energies and migration barriers, thereby facilitating defect recombination and regulating defect migration [2]. Meanwhile, interlayer interfaces promote the recombination of opposite types of point defects, which in turn reduces the accumulated defect density [7].

Accordingly, the layer interface characteristics of Cu/MEA are investigated. In each MEA layer, the nanocrystals with average width of 35 nm are observed and the grain boundaries are marked by blue lines in Fig. 4(a), which leads to different crystallographic orientation relationships along the layer interfaces. From the FFT patterns, interface with relationship of $(01\bar{1})_{BCC} \parallel (1\bar{1}1)_{FCC}$, $[\bar{1}11]_{BCC} \parallel [011]_{FCC}$ (Type 1, K-S relationship) marked by yellow, and $(01\bar{1})_{BCC} \parallel (\bar{1}10)_{FCC}$, $[\bar{1}11]_{BCC} \parallel [001]_{FCC}$ (Type 2) marked by red, have been confirmed. Meanwhile, bubbles are more likely to form in front of the layer interfaces marked by yellow circles, whereas fewer bubbles are observed in front of those marked by red circles. Thus, it is plausible to hypothesize that the crystallographic orientation relationships of the FCC and BCC layer interfaces influence the bubble distribution. The magnified TEM image in Fig. 4(b) shows that the bubbles aggregate and grow in front of the K-S layer interface. Fig. 4(c) displays an obvious difference that a bubble appears in front of the K-S layer, however, no bubbles can be observed in front of the interface with the orientation relationship of $(01\bar{1})_{BCC} \parallel (\bar{1}10)_{FCC}$, $[\bar{1}11]_{BCC} \parallel [001]_{FCC}$. The schematic diagram of the bubble distribution tendency with the interface orientation relationship is shown in Fig. 4(d). Li et al. [48–52] have proposed that He atoms tend to be trapped by vacancies because of the low solubility of He in host materials. Therefore, the nucleation positions of the bubbles are significantly affected by the vacancy distribution. For the present MEA multilayer film, the energy variation associated with a vacancy migrating to various layer interfaces can provide insights into the bubble distribution tendency. The bubble morphology and distribution in the multi-principal alloys differentiate with most bimetal multilayers, and the irradiation resistance is also improved. The detailed mechanism of irradiation resistance is discussed in Supplementary 2.

In addition, the grain boundaries in each layer significantly influence the irradiation behavior. Notably, bubbles with relatively larger size are preferentially distributed along the Cu grain boundaries, as indicated by the pink arrows in Fig. 4(a). A similar phenomenon is observed in the Cu/Nb multilayer, where bubbles prefer to align along either the interface or a grain boundary. This spatial arrangement is attributed to the minimization of interfacial and grain boundary energy [43]. In contrast, within the TaNbMo layers, the irradiation temperature remains insufficient to facilitate complete vacancy diffusion, resulting in no discernible difference in bubble distribution between grain boundaries and grain interiors.

The dynamics of helium in the 5 nm Cu/TaNbMo multilayer were examined through the observation of helium bubble evolution. Fig. 5(a) presents a cross-sectional STEM image of the sample irradiated at 400 °C. Bubbles are observed to be distributed along the interfaces of all Cu layers, driven by the reduction of interface energy. Notably, no

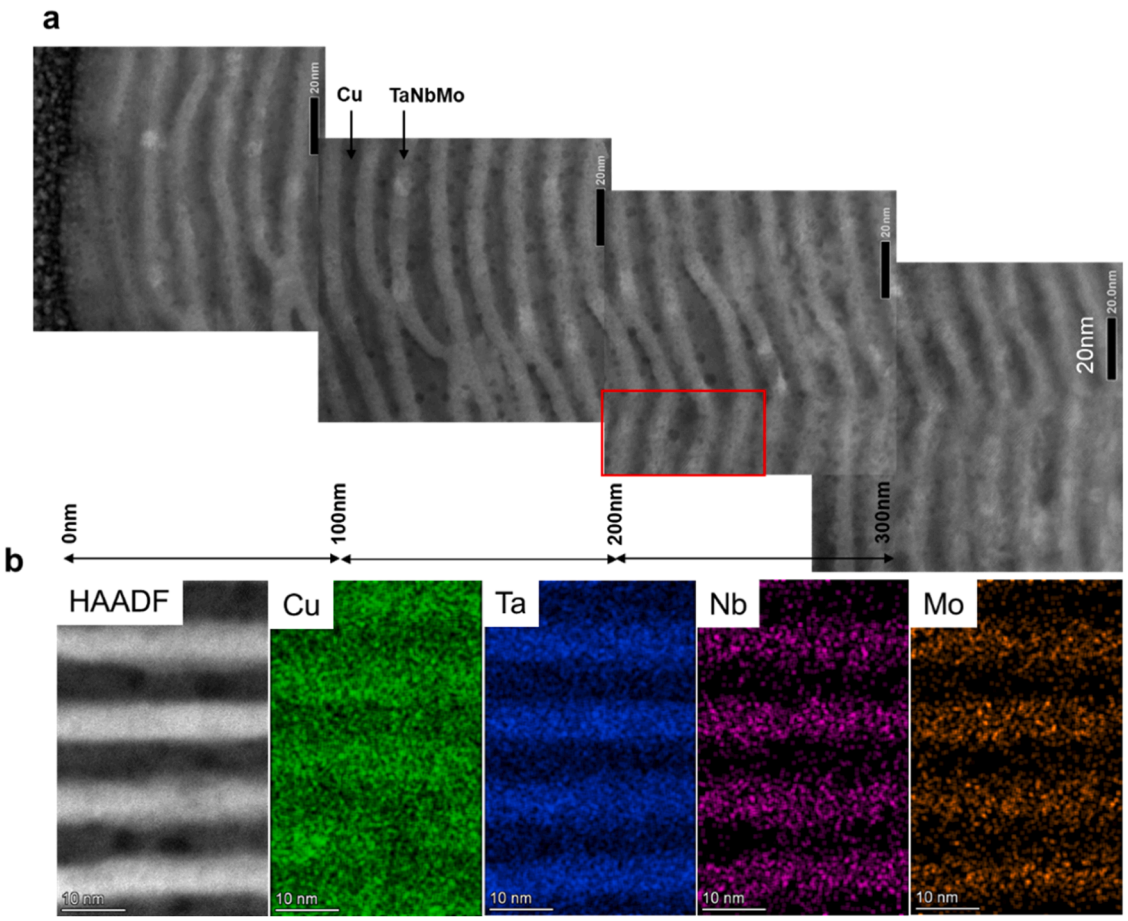

Fig. 5. Microstructure and EDS results of the 5 nm Cu/TaNbMo multilayer film after irradiated at 400 °C. (**a)** Cross-sectional bubble distribution, showing bubbles with diameter of approximately 1 nm dispersing both along the layer interfaces and inside the layers. (**b)** EDS mapping obtained from the area framed in a, showing that Cu diffuses into adjacent layers, while the Ta, Nb and Mo elements just show slight diffusion tendency.

statistically significant difference in bubble distribution density and size is detected between grain boundary regions and grain interiors. The dose peak of Cu layers appears at around 200–250 nm depth, in which area the bubble size reaches the largest value. In the TaNbMo layers, no obvious bubbles are observed within 150 nm depth to the irradiation surface, as confirmed by Fig. 5(a) and HRTEM images in Supplementary 3, suggesting that the helium concentration is insufficient for the nucleation cores to develop into stable bubbles. At a depth between 150–300 nm, minute bubbles with diameter of approximately 1 nm are observed, distributing both along the layer interfaces and inside the layers. EDS mapping across the 200–250 nm depth reveals that irradiation induces Cu diffusion into neighboring layers, whereas Ta, Nb, and Mo exhibit only a slight diffusion tendency. This phenomenon is commonly observed in Cu/Fe [53], W/Ni [54] multilayers, since the large compactness of FCC structure of Cu layers inhibits the inward diffusion of elements from adjacent layers. In contrast, the TaNbMo layers with BCC structure exhibit larger interstitial spaces that facilitate inward diffusion. Additionally, the melting points of these metals significantly influence their diffusion behavior. Cu element, with a relatively low melting point (~1085 °C), contrasts with Ta (~3017 °C), Nb (~2477 °C), and Mo (~2610 °C), whose higher melting points are typically associated with lower atomic mobility. Moreover, the smaller atomic radius of Cu element (1.28 Å) compared to Ta (1.46 Å), Nb (1.46 Å), and Mo (1.39 Å) enhances its diffusion and solubility when these metals intermix. The atomic size mismatch in the TaNbMo layers may, however, create additional barriers to diffusion for the heavier transition metals.

Bubbles within the Cu layers of samples irradiated at both 300 °C and 400 °C are observed to distribute along the layer interfaces, a pattern consistent with previous findings in Cu/Mo and Cu/Co multilayer films [55–57]. Consequently, a high concentration of vacancies is produced at the interfaces, trapping helium atoms and facilitating bubble nucleation sites. As the irradiation temperature rises to 400 °C, the helium diffusion rate accelerates, resulting in more helium atoms being trapped by vacancies and enhancing bubble nucleation.

The magnified microstructures of 5 nm multilayer film in depth of 100–150 nm and 150–200 nm are shown in Fig. 6. At the depth of 150–200 nm, some bubbles growing up throughout the entire thickness of the Cu layer can be observed. With increasing irradiation temperature, both bubble size and density within the Cu layers at a given depth are increasing. The enhanced He diffusion ability facilitates their absorption by vacancies, further promoting bubble nucleation. However, for the TaNbMo layers, irradiation temperature is insufficient for rapid bubble growth, thus the bubbles are in the early stages of nucleation. Consequently, across all irradiated areas, bubble size is around 1 nm independent of irradiation depth. Furthermore, an increase in irradiation temperature also results in a higher bubble density, a trend that aligns with observations in the Cu layers. The bubble size and density in the damage peak regions of films with different thicknesses and irradiation temperatures are concluded in Fig. 6e and f (Table 2).

3.3. *Irradiation-induced hardening*

Fig. 7(a) compares the average nano-indentation hardness of the Cu/TaNbMo multilayer films with modulation period of 5 nm and 50 nm before and after irradiated at 300 °C and 400 °C. For the as-deposited

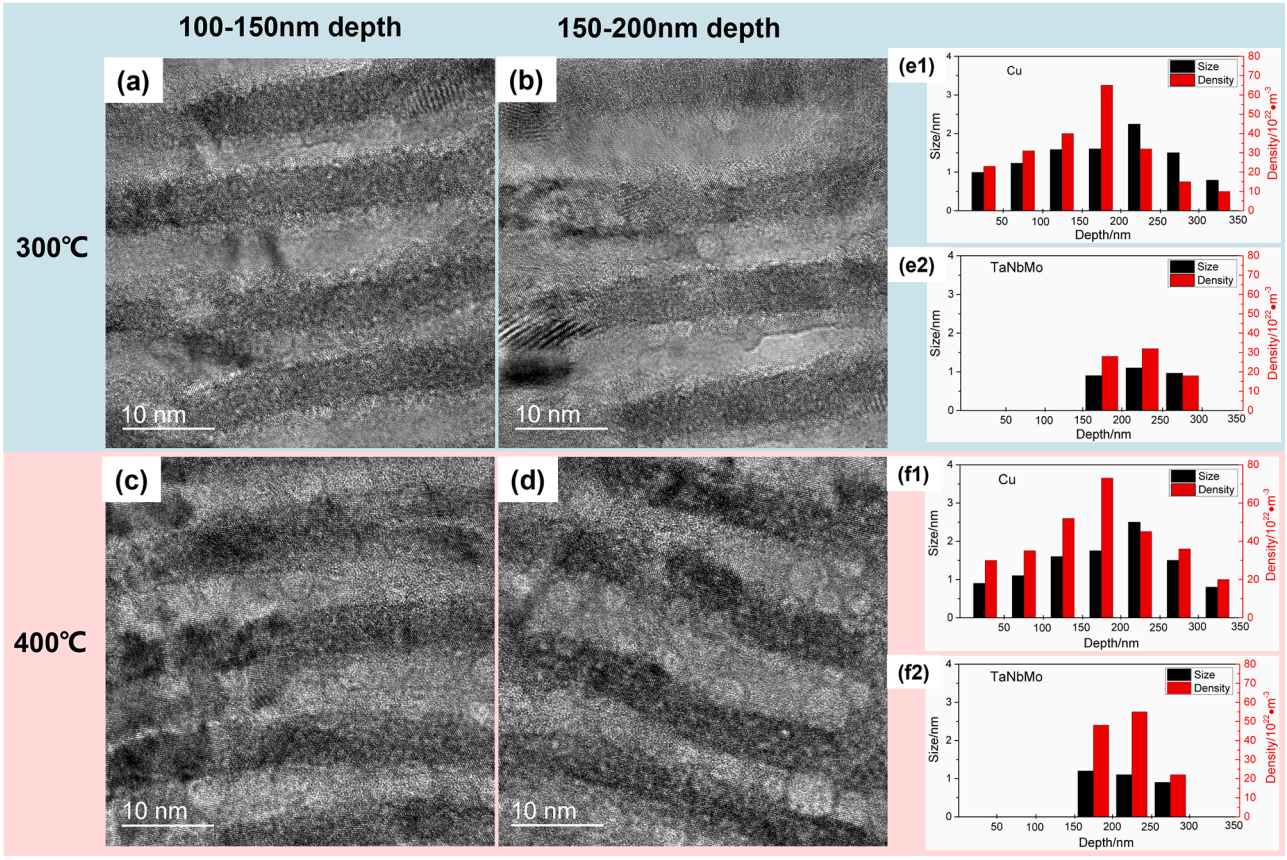

Fig. 6. Cross-sectional TEM images and He bubble distribution of the 5 nm Cu/TaNbMo multilayer films after He irradiation. **(a-d)** Bubble distribution at 100–150 and 150–200 nm depth after irradiated at 300 °C and 400 °C, respectively, a diverse range of bubble sizes is observed within the Cu layers depending on the irradiation temperature and depth, while bubbles around 1 nm are prominent in the TaNbMo layers. **(e1-f2)** Average density and size distribution of the bubbles after irradiated at 300 °C and 400 °C, respectively.

Table 2
Bubble size and density of Cu layer and MEA layer in the damage peak regions including films with different thicknesses and irradiation temperatures.

	5 nm 300 °C	5 nm 400 °C	50 nm 300 °C	50 nm 400 °C
Size (Cu, nm)	1.6	1.8	3.8	4.4
Density (Cu, 10^{22}/ m^3)	65.2	73.3	18.2	16.7
Size (MEA, nm)	0.9	1.1	0.9	1.1
Density (MEA, 10^{22}/ m^3)	28.1	48.0	55.8	60.3

multilayers, the hardness H is 4.9 and 6.8 GPa, corresponding to 50 and 5 nm multilayers. The irradiation hardening in 50 and 5 nm multilayers is around 1 GPa and 0.4 GPa, respectively. The hardening effects are similar for samples irradiated at both 300 °C and 400 °C. The irradiation-induced hardening is gradually suppressed with decreasing modulation period, in agreement with prior studies on irradiated bimetallic multilayers [57]. This phenomenon can be attributed to the role of layer interfaces as efficient sinks for irradiation-induced defects, such as vacancies and interstitials. At reduced modulation period, the high interface density promotes the annihilation of most defects at interfaces prior to their stabilization into clusters. Consequently, fewer residual defects remain within the layer to impede dislocation motion, leading to a reduction in hardening. Moreover, the MEA multilayer films exhibit less irradiation-induced hardening compared to most bimetal multilayer films, as illustrated in the comparative image of Fig. 7(b).

The initial observations indicate that the hardness and elastic modulus of MEA films increase after irradiation, attributing to the presence of these He bubbles. The classical Friedel–Kroupa–Hirsch (FKH) model [63] offers an approach to comprehend the interaction between dislocations and point defects, suggesting that the rise in yield strength ($\Delta\sigma_y$) is directly proportional to the increase in applied stress to move a dislocation line through an obstacle field. However, the application of FKH model to the irradiated MEA films reveals a significant discrepancy between the calculated and experimental hardness values. The calculated hardness increase is 0.12 GPa, which is far less than the experimentally obtained increase of 1 GPa. This discrepancy suggests that the FKH model may not fully account for the complex layer structure of the MEA films.

To address this issue, Yu et al. [13] proposed a more sophisticated model that considering the interplay between the separation distance of He bubbles (L) and the layer thickness (h), expressed as below:

$$\Delta\tau \cdot b \cdot (h-d) = 2W_L \cdot n \tag{4}$$

Where $n = \frac{h}{L}$, is the number of dislocation segments within one layer. W_L is the dislocation bowing energy induced by adjacent He bubbles. For a 60° mixed dislocation, W_L can by estimated as:

$$W_L = \frac{\mu b^2}{16\pi}\left(\frac{4-\upsilon}{1-\upsilon}\right) ln\frac{h'}{b} \tag{5}$$

Where υ is Poisson's ratio (0.34) and h' is the effective layer thickness. Therefore, Eq. (4) can be expressed as:

$$\Delta\tau = \frac{\mu b}{8\pi}\left(\frac{4-\upsilon}{1-\upsilon}\right)\frac{1}{(h-d)}\frac{h}{L} \cdot ln\frac{h'}{b} \tag{6}$$

This model posits that when the layer thickness is significantly larger

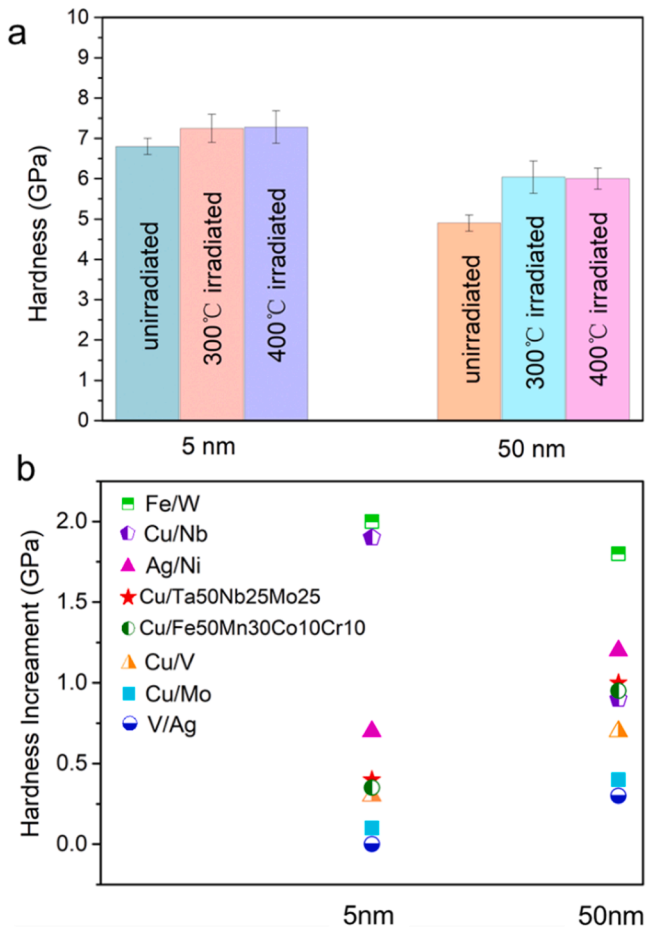

Fig. 7. Hardness and irradiation-induced hardening of the Cu/TaNbMo multilayer films. **(a)** Hardness before and after irradiation, indicating the irradiation hardening in 50 and 5 nm multilayers is around 1 GPa and 0.4 GPa. **(b)** Hardness increment after He ion irradiation, including bimetal multilayer Fe/W [58], Cu/Nb [59], Ag/Ni [60], Cu/Fe50Mn30Co10Cr10 [61], Cu/V [17], Cu/Mo [62], V/Ag [57]. MEA multilayer films exhibit less irradiation-induced hardening compared to most bimetal multilayer films.

than the separation distance of the bubbles ($h/L > 2$), the additional shear stress ($\Delta\tau$) required for dislocations to propagate through the bubble array can be calculated using a specific formula. The model specially considers the dislocation bowing energy induced by adjacent He bubbles, which is crucial for understanding the interaction between dislocations and bubbles.

The revised model, which incorporates the layer structure and the effect of He bubble separation, provides a hardness value of 1.097 GPa, which is in good agreement with experimental data, suggesting that the model is more effective in capturing the essence of irradiation hardening in MEA films.

However, when the layer thickness is <10 nm (or less than the separation distance of the bubbles), the hardening from He bubbles is estimated by:

$$\Delta\tau = \frac{\mu b}{8\pi L}\left(\frac{4-\upsilon}{1-\upsilon}\right) ln\frac{h}{b} \tag{7}$$

The model predicts a hardness increment of 0.6 GPa, which is higher than the experimental results. This overestimation may arise from the assumption that He bubbles act as hard obstacles to dislocations. In reality, dislocations can penetrate through He bubbles and voids [64], which means that the assumption of hard obstacles may bring in errors, especially at high bubble densities.

While the FKH model provides a fundamental understanding of irradiation hardening, it might not fit for the MEA multilayer films. In this case, the layer structure and the actual interaction between dislocations and He bubbles should be explicitly modeled for a more accurate prediction of hardness changes in irradiated MEA films. The model proposed by Yu et al. is a significant advancement in this direction, offering a more nuanced approach to understand the complex interplay among the irradiation-induced defects.

3.4. Bubble distribution along layer interfaces

To elucidate the bubble distribution tendency, the formation energies and the average segregation energy of a single vacancy near two types of Ta/Cu interfaces was calculated at first, with the results presented in Fig. 8. The formation energies of vacancies in the bulk region of Ta and Cu were 3.06 eV and 1.27 eV, respectively, consistent with the previous works [65–67]. The substantially lower vacancy formation energy in Cu compared to Ta implies a higher propensity for vacancies or voids to form within Cu lattices, corroborating experimental observations of predominantly Cu-based bubble formation.

This study constructs two types of layer interfaces: the K-S relationship, designated as Type 1, and the alternative orientation relationship, designated as Type 2. Type 1 interfaces feature a greater number of sites with vacancy formation energies below zero compared to Type 2, and the interface width (~2 nm) that traps vacancies is wider for Type 1 (refer to Fig. 8(a-d)). Furthermore, both the formation energy and average segregation energy for Type 1 are lower than those for Type 2 (refer to Fig. 8(e)). This suggests that Cu vacancies are thermodynamically favored to aggregate at Type 1 interfaces. Indeed, the K-S interface represents a typical semi-coherent interface characterized by misfit dislocations that originate from excess half-atomic planes [68]. Within the K-S interface, misfit dislocations induce localized lattice strain, and notably, vacancy formation at these dislocation sites can effectively relieve such strain—a process that in turn lowers the overall energy barrier for vacancy generation.

The average formation energy of Cu vacancy clusters at Type 1 and Type 2 interfaces is further calculated (Fig. 9), the results are analyzed comparing with that in bulk Cu. The average formation energy of vacancy clusters (E_f) in Type 1 is lower than that in Type 2, which is consistent with the trend of the monovacancy, suggesting that vacancies tend to form at the Type 1 interface. Specifically, E_f in both Type 1 and Type 2 is lower than that in bulk, and the values increase with the number of vacancies. E_f in Type 2 is always higher than that in Type 1.

Interestingly, E_f in Type 1 is less than zero when the number of the vacancy <200. Conversely, for Type 2, E_f is relatively high (> 0.2 eV) before the number exceeds 200. However, the segregation behavior of vacancies near the interfaces, as illustrated in the subfigures of Fig. 9, reveals that large vacancy clusters first form near the Type 2 interface when the total number of vacancies reaches approximately 500 (see Fig. 9, Subfigure IV). In these subfigures, each yellow dot denotes a single vacancy. This suggests that Type 2 has reached a relative saturation in absorbing vacancies, and vacancies are precipitated in the bulk region near Cu because vacancies are forced into the simulation box. When the total vacancies exceed 500, the average formation energy of vacancies in Type 2 approaches that of the bulk vacancy clusters (~0.3 eV). Vacancies will preferentially form in regions with lower formation energies and a higher number of trapping sites. From a thermodynamic standpoint, vacancies are more likely to segregate near Type 1 interfaces over Type 2, acting as precursors for bubble nucleation.

4. Conclusions

In summary, a systematic investigation of the microstructural and mechanical property evolution in Cu/TaNbMo medium-entropy multilayer films following 60 keV He ion irradiation, employing both experimental and molecular dynamics simulation approaches is presented. The hetero phase interfaces between Cu and TaNbMo act as defect sinks,

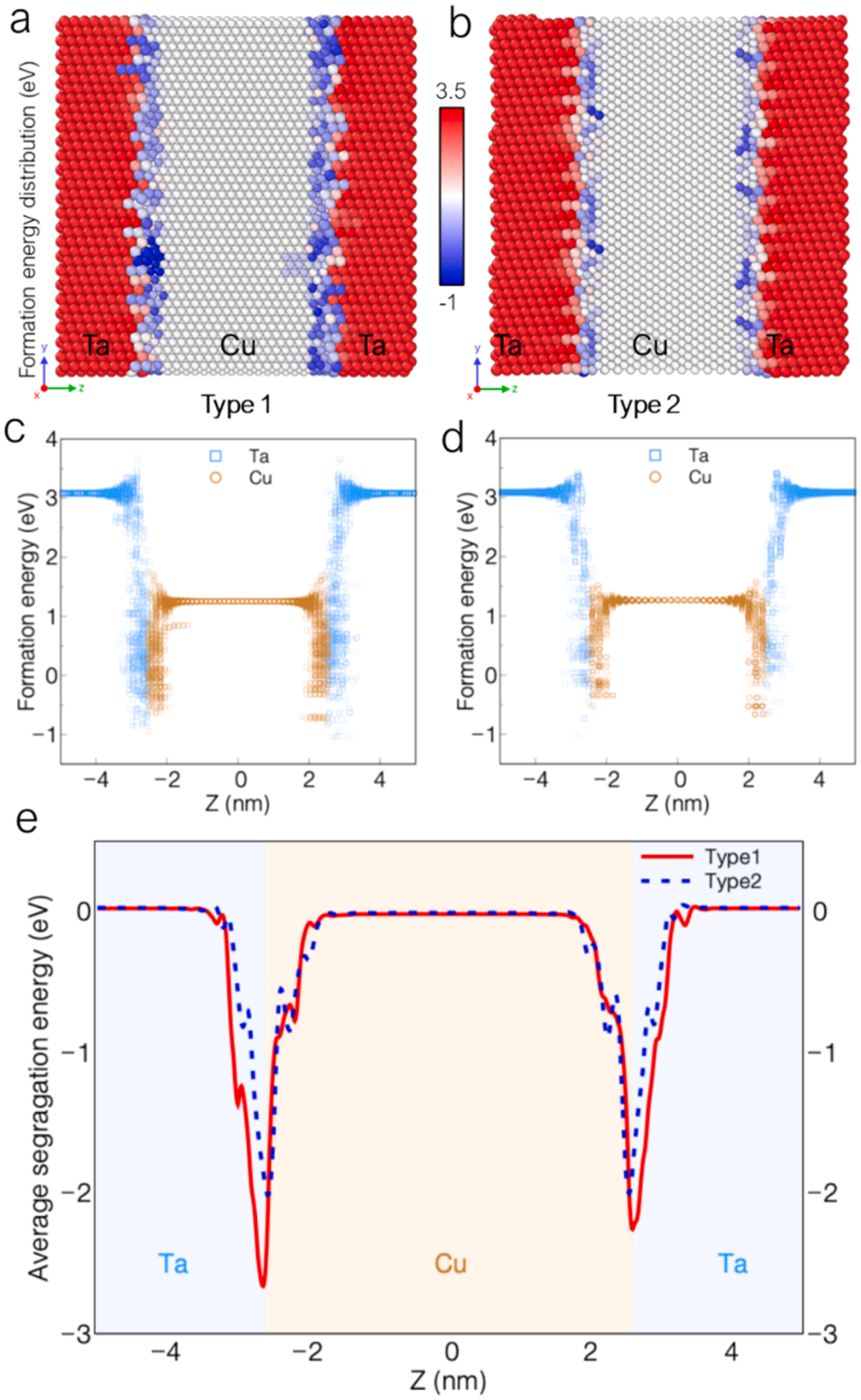

Fig. 8. Formation and segregation energies of a vacancy in Ta/Cu interfaces of Type 1 and Type 2. **(a, b)** Distribution of vacancy formation energy in Ta/Cu interfaces. (**c, d)** Vacancy formation energy varying with the displacement relative to the interfaces. (**e**) Vacancy segregation energy varying with the displacement to the interfaces. Scales along Z direction in (a-d) are identical.

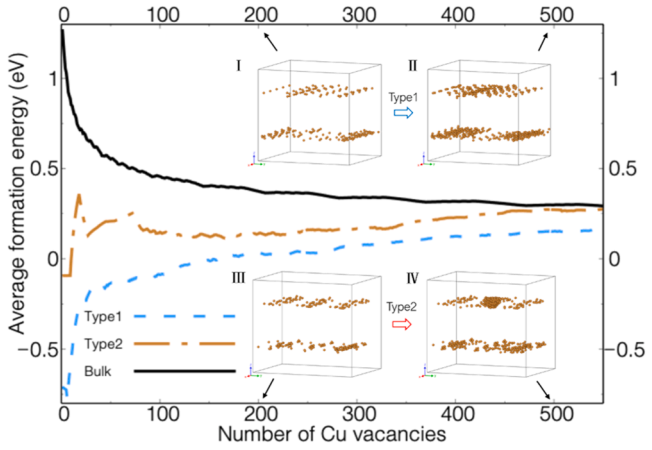

Fig. 9. Average formation energy of Cu vacancies at the Ta/Cu interfaces with varying the number of vacancies. Bulk indicates the average formation energy of the vacancy cluster in FCC Cu. The average formation energy of Cu vacancy clusters at Type 1 is lower than that of Type 2 and bulk Cu.

facilitating annihilation and recombination, resulting in enhanced irradiation tolerance for Cu/TaNbMo multilayers with 5 nm layer thickness, characterized by low bubble density and small size. The bubbles tend to distribute along Type 1 (K-S: $(01\bar{1})_{BCC} \parallel (1\bar{1}1)_{FCC}$, $[\bar{1}11]_{BCC} \parallel [011]_{FCC}$) interface in Cu layers. In the Type 1, there are more sites where the vacancy formation energy is less than zero compared to Type 2, and the width of the interface (~2 nm) that traps vacancies is broader than that of Type 2 (~1 nm). In addition, the average segregation energy is lower in Type 1 (−2.8 eV) than those in Type 2 (−2 eV), indicating that Cu vacancies are thermodynamically more inclined to aggregate at the Type 1 interface. These findings are expected to provide valuable insights into the control of irradiation-induced defects in multilayer film materials and offer a basis for expanding the design strategies of irradiation-resistant materials.

CRediT authorship contribution statement

Li Jiang: Writing – original draft, Project administration, Formal analysis. **Jiannan Hao:** Software, Formal analysis. **Guanzhi Wang:** Methodology, Data curation. **Guang Ran:** Validation, Methodology. **Yanhui Li:** Visualization, Data curation. **Qing Peng:** Writing – review & editing, Supervision, Software. **Wei Zhang:** Writing – review & editing, Supervision. **Lumin Wang:** Writing – review & editing, Resources.

Declaration of competing interest

The authors declare that they have no known competing financial interests or personal relationships that could have appeared to influence the work reported in this paper.

Acknowledgements

Authors acknowledge discussion with Professor Amit Misra in University of Michigan. Authors acknowledge the support provided by Science and Technology Planning Project of Liaoning Province (2023JH2/101700280), National Natural Science Foundation of China (Grant No 52571033, No 52101036, No 12272378), High-level Innovation Research Institute Program of Guangdong Province No 2020B0909010003, and LiYing Program of the Institute of Mechanics, Chinese Academy of Sciences (Grant No E1Z1011001). Authors acknowledge the assistance of DUT Instrumental Analysis Center.

Supplementary materials

Supplementary material associated with this article can be found, in the online version, at doi:10.1016/j.jnucmat.2025.156207.

Data availability

Data will be made available on request.

References

[1] S.J. Zinkle, et al., Materials challenges in nuclear energy, Acta Mater. 61 (2013) 735–758.
[2] Y. Zhang, et al., Influence of chemical disorder on energy dissipation and defect evolution in concentrated solid solution alloys, Nat. Commun. 6 (2015) 8736.
[3] Z. Chen, et al., A comparative study on the in-situ helium irradiation behavior of tungsten: coarse grain vs. nanocrystalline grain, Acta Mater. 147 (2018) 100–112.
[4] Z. Fan, et al., Helium irradiated cavity formation and defect energetics in Ni-based binary single-phase concentrated solid solution alloys, Acta Mater. 164 (2019) 283–292.
[5] W. Qin, et al., Microstructure and hardness evolution of nanochannel W films irradiated by helium at high temperature, J. Nucl. Mater. 502 (2018) 132–140.
[6] Z. Zhang, et al., Evaluation of helium effect on ion-irradiation hardening in pure tungsten by nano-indentation method, Nucl. Mater. Energy. 9 (2016) 539–546.
[7] I.J. Beyerlein, et al., Defect-interface interactions, Prog. Mater. Sci. 74 (2015) 125–210.
[8] X.M. Bai, et al., Efficient annealing of radiation damage near grain boundaries via interstitial emission, Science (1979) 327 (2010) 1631–1634.
[9] J. Wang, et al., Xe-ion-irradiation-induced structural transitions and elemental diffusion in high-entropy alloy and nitride thin-film multilayers, Mate. Des. 219 (2022) 110749.
[10] M. Wang, et al., Defect-interface interactions in irradiated Cu/Ag nanocomposites, Acta Mater. 160 (2018) 211–223.
[11] J. Wang, et al., Structural stability under Xe-ion irradiation of TiZrNbTaV-based high-entropy alloy and nitride films, Surf. Coat. Technol. 454 (2023) 129198.
[12] Z.J. Zhang, et al., Simultaneous enhancement in hardness and He-irradiation tolerance of TiVCr/W medium entropy nanolaminates, J. Alloys. Compd. 935 (2023) 168114.
[13] K.Y. Yu, et al., Superior tolerance of Ag/Ni multilayers against Kr ion irradiation: an in-situ study, Phil. mag. 93 (2013) 3547–3562.
[14] A. Misra, et al., The radiation damage tolerance of ultra-high strength nanolayered composites, JOM 59 (2007) 62–65.
[15] X. Zhang, et al., Nanostructured Cu/Nb multilayers subjected to helium ion-irradiation, Nucl. Instrum. Meth. B. 261 (2007) 1129–1132.
[16] M. Zhernenkov, et al., Trapping of implanted He at Cu/Nb interfaces measured by neutron reflectometry, Appl. Phys. Lett. 98 (2011) 241913.
[17] E.G. Fu, et al., Interface enabled defects reduction in helium ion irradiated Cu/V nanolayers, J. Nucl. Mater. 407 (2010) 178–188.
[18] E.G. Fu, et al., Fluence-dependent radiation damage in helium (He) ion-irradiated Cu/V multilayers, Phil. Mag. 93 (2013) 883–898.
[19] B. Cantor, et al., Microstructural development in equiatomic multicomponent alloys, Mater. Sci. Eng. A. 375 (2004) 213–218.
[20] S. Chen, et al., Short-range ordering alters the dislocation nucleation and propagation in refractory high-entropy alloys, Mater. Today 65 (2023) 14–25.
[21] M. Li, et al., A novel entropy-stabilized oxide coating thermally grown from a valve metal-based complex concentrated alloy, Mater. Today 74 (2024) 46–57.
[22] Z. Wang, et al., Solving oxygen embrittlement of refractory high-entropy alloy via grain boundary engineering, Mater. Today 54 (2022) 83–89.
[23] W. Qi, et al., Effects of Al and Ti co-doping on the strength-ductility- corrosion resistance of CoCrFeNi-AlTi high-entropy alloys, J. Alloys. Compd. 925 (2022) 166751.
[24] Z. Xu, et al., Corrosion resistance enhancement of CoCrFeMnNi high-entropy alloy fabricated by additive manufacturing, Corros. Sci. 177 (2020) 108954.
[25] B.X. Cao, et al., A novel L12-strengthened multicomponent Co-rich high-entropy alloy with both high γ′-solvus temperature and superior high-temperature strength, Scr. Mater. 199 (2021) 113826.
[26] T. Cheng, et al., Enhanced resistance to helium irradiations through unusual interaction between high-entropy-alloy and helium, Acta Mater. 248 (2023) 118765.
[27] C. Lu, et al., Enhancing radiation tolerance by controlling defect mobility and migration pathways in multicomponent single-phase alloys, Nat. Commun. 7 (2016) 13564.
[28] L. Jiang, et al., Irradiation-induced extremes create hierarchical face-/body-centered-cubic phases in nanostructured high entropy alloys, Adv. Mater. 32 (2020) e2002652.
[29] L. Yang, et al., High He-ion irradiation resistance of CrMnFeCoNi high-entropy alloy revealed by comparison study with Ni and 304SS, J. Mater. Sci. Technol. 35 (2019) 300–305.
[30] O. El-Atwani, et al., Helium implantation damage resistance in nanocrystalline W-Ta-V-Cr high entropy alloys, Mater. Today Energy 19 (2021) 100599.
[31] L. Jiang, et al., Microstructure and mechanical properties of nanoscale Cu/(Ta50Nb25Mo25) multilayers, Mater. Sci. Eng. A. 799 (2021) 140200.

[32] F. Kroupa, et al., Elastic interaction between prismatic dislocation loops and straight dislocations, Disc. Faraday Soc. 38 (1964) 49–55.
[33] D.J. Bacon, et al., Dislocation–obstacle interactions at the atomic level, Dislocations in solids 15 (2009) 1–90.
[34] B. Medasani, M. Haranczyk, A. Canning, et al., Vacancy formation energies in metals: a comparison of MetaGGA with LDA and GGA exchange–correlation functionals, Comput. Mater. Sci. 101 (2015) 96–107.
[35] W.J. Weber, et al., Predicting damage production in monoatomic and multi-elemental targets using stopping and range of ions in matter code: challenges and recommendations, Curr. Opin. Solid. State Mater. Sci. 23 (2019) 100757.
[36] M.J. Norgett, et al., A proposed method of calculating displacement dose rates, Nucl. Eng. Des. 33 (1975) 50–54.
[37] S. Plimpton, Fast parallel algorithms for short-range molecular dynamics, J. Comput. Phys. 117 (1995) 1–19.
[38] G.P. Pun, et al., Angular-dependent interatomic potential for the Cu–Ta system and its application to structural stability of nano-crystalline alloys, Acta Mater. 100 (2015) 377–391.
[39] R. Kumar, et al., Interface microstructure effects on dynamic failure behavior of layered Cu/Ta microstructures, Sci. Rep. 13 (2023) 11365.
[40] J. Chen, et al., Unraveling the role of interfaces on the spall failure of Cu/Ta multilayered systems, Sci. Rep. 10 (2020) 208.
[41] I.N. Mastorakos, et al., Deformation mechanisms and strength in nanoscale multilayer metallic composites with coherent and incoherent interfaces, Appl. Phys. Lett. 94 (2009) 173114.
[42] L.J. Perryman, et al., Cavity growth mechanism maps for reactor materials, J. Nucl. Mater. 165 (1989) 110–121.
[43] K. Hattar, et al., Arrest of He bubble growth in Cu–Nb multilayer nanocomposites, Scr. Mater. 58 (2008) 541–544.
[44] G.S. Was, Irradiation-induced voids and bubbles. Fundamentals of Radiation Materials Science: Metals and Alloys, Springer New York, New York, NY, 2016, pp. 379–484.
[45] J. Choi, et al., Equilibrium shape of internal cavities in sapphire, J. Am. Ceram. Soc. 80 (1997) 62–68.
[46] M. Wang, et al., Defect-interface interactions in irradiated Cu/Ag nanocomposites, Acta Mater. 160 (2018) 211–223.
[47] B.D. Todd, et al., Surface and bulk properties of metals modelled with Sutton-Chen potentials, Surf. Sci. 281 (1993) 191–206.
[48] Y. Li, et al., In-situ TEM investigation of 30 keV he^{+} irradiated tungsten: effects of temperature, fluence, and sample thickness on dislocation loop evolution, Acta Mater. 206 (2021) 116618.
[49] M. AbdElKeriem, et al., Helium-vacancy interaction in tungsten, Phys. Rev. B Condens. Matter. 47 (1993) 14771–14777.
[50] D. Perez, et al., The mobility of small vacancy/helium complexes in tungsten and its impact on retention in fusion-relevant conditions, Sci. Rep. 7 (2017) 2522.
[51] P.E. Lhuillier, et al., Helium retention and early stages of helium-vacancy complexes formation in low energy helium-implanted tungsten, J. Nucl. Mater. 433 (2013) 305–313.
[52] L. Jiang, et al., Elucidating He-H assisted cavity evolution in alpha Cr under multiple ion beam irradiation, Scr. Mater. 187 (2020) 291–295.
[53] Y. Chen, et al., Enhanced radiation tolerance in immiscible Cu/Fe multilayers with coherent and incoherent layer interfaces, J. Mater. Res. 30 (2015) 1300–1309.
[54] H. Chen, et al., The behavior of helium atoms in He^{+} ion implanted W/Ni bilayer nanocomposite, Appl. Surf. Sci. 486 (2019) 274–280.
[55] N. Li, et al., The influence of interfaces on the formation of bubbles in He-ion-irradiated Cu/Mo nanolayers, Philos. Mag. Lett. 91 (2011) 18–28.
[56] Y. Chen, et al., Unusual size-dependent strengthening mechanisms in helium ion-irradiated immiscible coherent Cu/Co nanolayers, Acta Mater. 84 (2015) 393–404.
[57] Q.M. Wei, et al., Suppression of irradiation hardening in nanoscale V/Ag multilayers, Acta Mater. 59 (2011) 6331–6340.
[58] N. Li, et al., He ion irradiation damage in Fe/W nanolayer films, J. Nucl. Mater. 389 (2009) 233–238.
[59] N. Li, et al., Defect structures and hardening mechanisms in high dose helium ion implanted Cu and Cu/Nb multilayer thin films, Int. J. Plast. 32-33 (2012) 1–16.
[60] K.Y. Yu, et al., Comparisons of radiation damage in He ion and proton irradiated immiscible Ag/Ni nanolayers, J. Nucl. Mater. 440 (2013) 310–318.
[61] Y.F. Zhao, et al., Unusual He-ion irradiation strengthening and inverse layer thickness-dependent strain rate sensitivity in transformable high-entropy alloy/metal nanolaminates: a comparison of Fe50Mn30Co10Cr10/Cu vs Fe50Mn30Co10Ni10/Cu, J. Mater. Sci. Technol. 116 (2022) 199–213.
[62] J.Y. Zhang, et al., Size-dependent plastic deformation characteristics in He-irradiated nanostructured Cu/Mo multilayers: competition between dislocation-boundary and dislocation-bubble interactions, Mater. Sci. Eng. A. 673 (2016) 530–540.
[63] F. Kroupa, et al., Elastic interaction between prismatic dislocation loops and straight dislocations, Disc. Faraday Soc. 38 (1964) 49–55.
[64] D.J. Bacon, et al., Dislocation–obstacle interactions at the atomic level, Dislocations in solids 15 (2009) 1–90.
[65] H. Fukushima, et al., The formation energies of a vacancy in pure Cu, Cu-Si, Cu-Ga and Cu- gamma Mn solid solutions by positron annihilation, J. Phys. F. 6 (1976) 677–685.
[66] P. Soederlind, et al., First-principles formation energies of monovacancies in bcc transition metals, Phys. Rev. B Condens. Matter. 61 (2000).
[67] S. Mukherjee, et al., Vacancy formation enthalpy at high pressures in tantalum, J. Condens. Matter. Phys. 15 (2003) 855–861.
[68] T. Tomida, Variant selection mechanism by elastic anisotropy and double KS relation for transformation texture in steel, Acta. Mater. 146 (2018) 25–41.